ADVANCED OPTICAL MATERIALS
www.advopticalmat.de

Check for updates

Room Temperature Phase Transition of W-Doped VO_2 by Atomic Layer Deposition on 200 mm Si Wafers and Flexible Substrates

Kai Sun, Callum Wheeler, James A. Hillier, Sheng Ye, Ioannis Zeimpekis, Alessandro Urbani, Nikolaos Kalfagiannis, Otto L. Muskens,* and Cornelis H. (Kees) de Groot**

The unique structural transition of VO_2 between dielectric and metallic phases has significant potential in optical and electrical applications ranging from volatile switches and neuromorphic computing to smart devices for thermochromic control and radiative cooling. Critical condition for their widespread implementation is scalable deposition method and reduction of the phase transition to near room temperature. Here, a W:VO_2 process based on atomic layer deposition (ALD) is presented that enables precise control of W-doping at the few percent level, resulting in a viable controllable process with sufficient W incorporation into VO_2 to reduce the phase transition to room temperature. It is demonstrated that the incorporation of 1.63 at.% W through ALD growth leads to a state-of-the-art phase transition at 32 °C with emissivity contrast between the low-temperature and high-temperature phase exceeding 40% in a metasurface-based radiative cooling device configuration. The process is shown to be viable on 200 mm silicon substrates as well as flexible polyimide films. The full and self-consistent temperature-dependent characterization of the W-doped VO_2 using spectroscopic ellipsometry, electrical conductivity, mid-wave infrared camera, and Fourier transform infrared emissivity, allows for a fully validated material model for the theoretical design of various smart and switchable device applications.

1. Introduction

Since its discovery in 1959,[1] Vanadium dioxide (VO_2) has been a widely studied material due to its well-known low-temperature thermochromic transition. This thermochromic transition involves a structural transition from an insulating monoclinic structure (VO_2 (M1)) at low temperature to a conducting rutile structure (VO_2(R)) at high temperature. The transition is accompanied by a similar change in optical response between dielectric and metallic which has recently generated numerous novel applications in smart windows,[2–9] passive radiative cooling applications,[10–13] neuromorphic computing,[14,15] volatile and nonvolatile memory,[16–18] reconfigurable antennas and optical system[19–21] and infrared identity management.[22–24]

VO_2 films have been synthesized by a wide range of deposition techniques, such as pulsed laser deposition,[25] sol-gel processing,[26] reactive sputtering,[4,27] epitaxy,[28] and atomic layer deposition

K. Sun, C. Wheeler, S. Ye, C. H. (Kees) de Groot
Electronics and Computer Science
Faculty of Engineering and Physical Sciences
University of Southampton
Southampton SO17 1BJ, UK
E-mail: k.sun@soton.ac.uk; chdg@soton.ac.uk

K. Sun, C. Wheeler, O. L. Muskens
Astronomy and Physics
Faculty of Engineering and Physical Sciences
University of Southampton
Southampton SO17 1BJ, UK
E-mail: o.muskens@soton.ac.uk

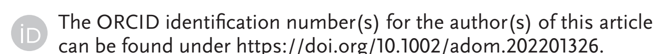
The ORCID identification number(s) for the author(s) of this article can be found under https://doi.org/10.1002/adom.202201326.

© 2022 The Authors. Advanced Optical Materials published by Wiley-VCH GmbH. This is an open access article under the terms of the Creative Commons Attribution License, which permits use, distribution and reproduction in any medium, provided the original work is properly cited.

DOI: 10.1002/adom.202201326

J. A. Hillier, N. Kalfagiannis
Department of Physics and Mathematics
School of Science and Technology
Nottingham Trent University
Nottingham NG11 8NS, UK

I. Zeimpekis
Optoelectronic Research Center
Faculty of Engineering and Physical Sciences
University of Southampton
Southampton SO17 1BJ, UK

A. Urbani
Consorzio C.R.E.O.
L'Aquila 1-67100, Italy

 © 2022 The Authors. Advanced Optical Materials published by Wiley-VCH GmbH

(ALD).[29–33] Among these techniques, ALD stands out as a deposition technique compatible with CMOS technology and large-area mass production. In particular, Peter et al. demonstrated that a sub-10 nm VO_2 continuous film can be formed on 300 mm diameter Si substrates with a clear transition capability in electrical properties.[29] However, the transition temperature of pure VO_2 is ≈68 °C[34,35] and thus nonideal for most applications which are targeted at operation around room temperature. Room temperature operation is important in order to minimize energy consumption in applications such as neuromorphic computing and volatile memory, while it is critical when using ambient temperature as a functional trigger, for example in radiative cooling and smart windows. To overcome the limitation of the elevated transition temperature of pure VO_2, various methods were used to reduce the transition temperature by introducing transition-metal dopants[36–39] such as W, Mg, Ta, Al, and Ti. The high valence dopants such as W disturb the electronic configuration of the V–V chain though the detailed mechanism is not yet clear.[40,41] Near room temperature metal-insulator transition has been achieved for W:VO_2 with the electrical/optical property contrast preserved, and advanced multilayers have been constructed to optimize thermal response.[23,42,43] The availability of a W:VO_2 ALD process would allow further control of the optical stack to improve both performance and scalability, and might be a key solution to unlock optical and electrical applications involving CMOS compatible technologies for large volume manufacture.

Here, we demonstrate the highly controlled fabrication of W:VO_2 materials at a range of W doping levels over 200 mm full wafer scale. We show that, despite a nearly 100-fold difference in growth rates between VO_2 and WO_3, a small temperature window exists where extreme precursor ratios of W/V lead to a viable controllable ALD process with sufficient W incorporation into the VO_2 to reduce the insulator to metal transition temperature to room temperature. We demonstrate uniform deposition on both 200 mm wafers and flexible polyimide substrate. We furthermore show that the transition temperature of the W:VO_2 films can be precisely controlled through the ratio of W and V cycles during the atomic layer deposition process. Detailed material and optical properties are reported as a function of W doping concentration and temperature, allowing the data to form a base for design and simulation of advanced smart optical applications.

As an example of the capability of the process, we demonstrate a variable-emissivity smart metasurface-based optical solar reflector (meta-OSR) on polyimide by lithographic patterning of the W:VO_2 film. OSRs are critical for the thermal management of satellites and spacecrafts. With a desired low solar spectrum absorption and a high infrared (IR) emissivity, OSRs are conventionally achieved using aluminum-coated glass tiles.[44] Recently thin-film metasurface-based OSRs were proposed for their advantage of low weight which significantly reduces satellite launch costs.[12,45,46] However, these meta-OSRs are breadboard devices on Si substrates and mechanical flexibility and robustness which significantly reduces assembly complexity for curved satellite surface would be a significant step for commercialization of the next generation meta-OSRs. We demonstrate here that our smart meta-OSRs with W doping can be formed on polyimide substrates and that the fabricated W:VO_2 meta-OSRs have passive thermal management capability through its high emissivity contrast and near room temperature transition, which is a significant step forward in upscaling capability and commercial potential.

2. Results and Discussion

2.1. Atomic Layer Deposition of W:VO_2

To establish a strategy for W:VO_2 deposition we start from the state of the art in VO_2 and WO_3 processes reported in the literature. Combining such processes turns out highly nontrivial due to the large difference in working points and process conditions which at first sight appear incompatible but in fact allow for a very narrow window of opportunity. Successful ALD processes for pure VO_2 based on $V(NEtMe)_4$ (TEMAV) have been reported in recent years by using either ozone[30–32,47] or water.[27,29,48,49] The optimized deposition temperature was determined as 150 °C, limited by the thermal decomposition of TEMAV. A WO_3 ALD process based on $W(CO)_6$ and water was first demonstrated by Mamun et al. at deposition temperatures ≈300 °C with a growth rate of 0.02 nm per cycle.[50] A WO_3 ALD process based on $W(CO)_6$ using ozone was achieved at about 200 °C with a growth rate of 0.02 nm per cycle.[51] With lower deposition temperatures, the growth rate was seen to decrease significantly for the ozone precursor.[51]

To achieve an ALD process for W-doped VO_2, an interleaved process setup is implemented as shown in **Figure 1**a. The growth rates for the individual deposition of VO_2 and WO_3 at 200 °C were found to be 0.054 nm per cycle and 0.006 nm per cycle, respectively. The growth rate of VO_2 is consistent with reported values.[52] The WO_3 growth rate is further reduced in the presence of a VO_2 matrix, and W/V precursor ratios approaching unity are required to achieve even a 1 at.% W-doping as will be shown below. The total number of TEMAV cycles was fixed with a varied $W(CO)_6$ cycle number. Different W/V cycle ratios of 0, 0.2, 0.6, 0.8, and 1.2 were used to achieve various W dopings (see details in Supporting Information S1). For each W/V cycle ratio, a thickness of ≈40 nm of W:VO_2 was deposited onto a 1100 nm SiO_2/100 nm Al stack on a Si substrate, The fabricated stack forms the metal-nsulator-metal (MIM) structure of an optical solar reflector (OSR) structure.[12,45] Cross-section SEM images are presented in Supporting Information Figure S2.

Figure 1b shows a photograph of the 200 mm Si wafer coated with a W:VO_2 deposited film on the 1100 nm SiO_2/80 nm Al stack, for the W/V cycle ratio of 0.8. The film color is uniform except for small deviations at the top and bottom edge, which are attributed to edge non-uniformity of SiO_2 growth in the sputtering system. The W:VO_2 film adhesion is excellent with no visible defect. Ellipsometry has been used to measure the uniformity with a fitted thickness map as shown in Figure 1c. The thickness uniformity, defined as the standard deviation over the average thickness, is calculated to be 4% over the 200 mm substrate. Extended information for both undoped and doped VO_2 films is detailed in Supporting Information S3.

© 2022 The Authors. Advanced Optical Materials published by Wiley-VCH GmbH

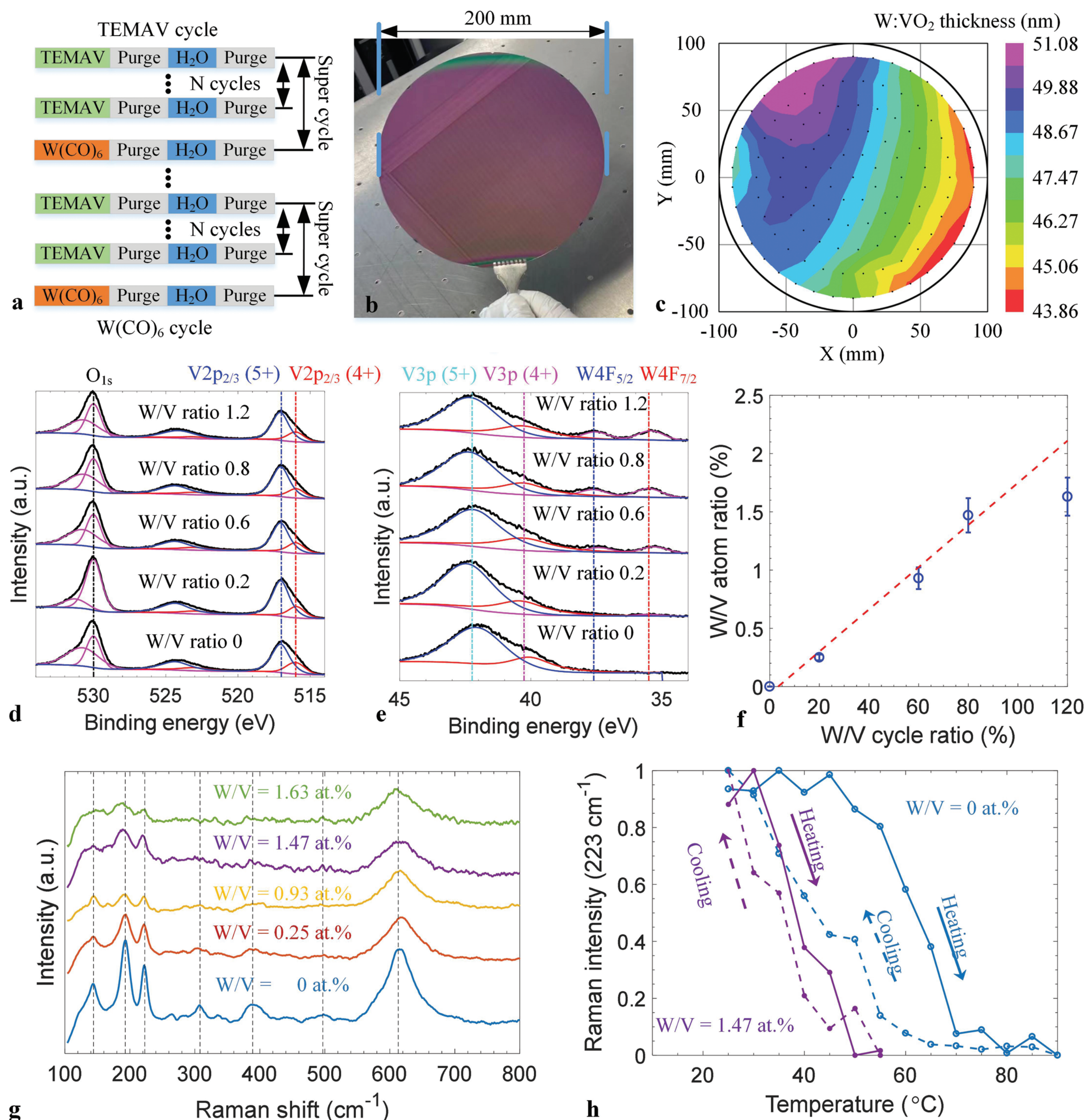

Figure 1. Atomic layer deposition and material characterizations of W-doped VO_2. a) ALD cycle growth configuration of W:VO_2. b) Optical Photograph of W:VO_2 film (W/V cycle ratio 0.8) on 200 mm substrate. c) W:VO_2 thickness mapping of the W:VO_2 (1.43 at.%) film fitted using a Vis/NIR ellipsometry. d) XPS spectra (high binding energy) for W:VO_2 films with different W contents, e) XPS spectra (low binding energy) for W:VO_2 films with different W contents, f) extracted W doping % from XPS spectra with the dashed line as a linear fit with data of W/V cycle ratio between 0 and 0.8. g) Room temperature Raman spectra of W:VO_2 grown with different W/V atomic ratios. h) Normalized Raman intensity of A1g peak at 223 cm^{-1} as a function of temperature for W/V atomic ratio of 0% and 1.47%.

For the as-deposited W:VO_2 films, X-ray photoelectron spectroscopy (XPS) was performed to extract the experimental W/V ratio in the films and the binding spectra for the vanadium range are shown in Figure 1d. The binding energy values are usually calibrated against the C1s peak at 284.8 eV. However, vanadium spectra can be more conveniently calibrated using the O1s peak at 530.0 eV as O1s peak is present in the vanadium measurement range[32,53,54] facilitating comparison with other VO_2 works. The vanadium, V2p energy level has the $V2p_{1/2}$ and $V2p_{3/2}$ components at 523.0 and 516.0 eV, for V4+ oxidation state, and 524.3 and 517.0 eV, for V5+ oxidation state, respectively.[53,55,56] For all the W/V cycle ratios from 0 to 1.2, the

© 2022 The Authors. Advanced Optical Materials published by Wiley-VCH GmbH

spectra are consistent with a mixture of V_2O_5 and VO_2, where W doping has an insignificant impact on the ratio between V_2O_5 and VO_2. The XPS spectra for tungsten are presented in Figure 1e. For W6+, the binding energies are calibrated using C1s at 284.8 eV, as it is normally done when analyzing this core level for both W and V peaks.[57,58] The W characteristic peaks are at binding energies of 35.4 and 37.6 eV for W4f7/2 and W4f5/2 doublets, respectively.[57] The V3p peaks can also be identified at binding energies of 40.3 and 42.3 eV for V4+ and V5+, respectively.[59,60]

In addition to the V2p orbitals, the V4+/V5+ ratios can also be extracted by fitting V3p peaks as part of the W4f and the ratios are consistent with those from V2p peak fittings (see Supporting Information Figure S4). For the 0.2 W/V cycle ratio, W peaks can be barely identified above the noise of the spectrum, indicating a low W content near the detection limit of the equipment. For higher W/V cycle ratios of 0.6, 0.8, and 1.2, W peaks can be easily identified at their established positions, with peak height increasing with W/V cycle ratio. Through peak area fitting of W4f and V3p, the W/V atomic ratio can be extracted and is plotted in Figure 1f as a function of W/V cycle ratio. The W/V atomic ratio increase is linear between W/V cycle ratio of 0–0.8 and then deviates from the extrapolation, indicating a further reduction in the efficiency of W incorporation into VO_2. A linear fit of the data between the 0–0.8 W/V cycle ratios indicates that the W/V coefficient is ≈0.01. Despite this extremely low W precursor efficiency, both the XPS data and subsequent optical data demonstrate that the W content in W:VO_2 can be accurately controlled through the tuning of W/V cycle ratio. The extracted W doping atomic percentages (at.%) from XPS, 0.25 at.%, 0.93 at.%, 1.47 at.%, and 1.63 at.%, are used in the rest of this work to denote the samples with W/V precursor ratios of 0.2, 0.6, 0.8, and 1.2, respectively.

As the as-deposited VO_2 (W:VO_2) films are amorphous, a post-anneal treatment is required to crystalize the VO_2 into monoclinic VO_2 (M1) to activate its thermochromic properties. The anneal condition requires a fine balance between temperature, oxygen pressure, and anneal time.[54] The optimization process for our films is detailed in Supporting Information Figure S6. The optimized W:VO_2 films here are all annealed in an O_2 pressure of 1.3×10^{-3} Pa for 2 h at 400 °C. All subsequent data is on annealed films.

Room temperature Raman spectroscopy is shown in Figure 1g. The characteristic Ag peaks of the V–V vibration at 192 cm^{-1} and 223 cm^{-1} are clearly visible together with the V–O Ag vibrational peak at 610 cm^{-1}. The other minor peaks are also consistent with the insulating monoclinic VO_2 phase.[61,62] The W-doped VO_2 shows identical peaks to the pure VO_2 phase although less pronounced. Temperature dependent Raman spectra were taken (see Supporting Information Figure S5) with the resulting monoclinic to rutile transition temperature extracted in Figure 1h. The reduction in transition temperature with W-doping is clearly demonstrated. All data has been taken at very low power to prevent accidental heating.

2.2. Optical Characterizations of W:VO_2

Spectroscopic ellipsometry was performed for all samples as a function of temperature to demonstrate the optical transition of the different films. **Figures 2**a–j present the resulting refractive index n and extinction coefficient k, respectively, for the VO_2 films grown with increasing W/V cycles ratio, for temperatures between 20 °C and 100 °C (dark red to purple lines; in rainbow order). The ellipsometry data were obtained in the cooling branch of the hysteresis curve, i.e. starting from the highest temperature and subsequently lowering the temperature.

To illustrate how the optical property changes with temperature, we show in Figure 2k,l values of n and k at 5 µm wavelength as a function of temperature. The IMT transition shifts to a lower temperature with W-doping, reaching near room temperature for the highest doping observed here. At low temperatures, prior to the onset of the IMT, a difference in the optical constants can be noted between the individual films due to the additional presence of W.[63,64] For the determination of the transition temperature, it is sufficient to note the variation in the optical constants from the sample measured at room temperature and above, where k increases with temperature. This is indicative of an increase in free carrier absorption related to the phase transition of VO_2.[63] It is also observed that the magnitude of the effect of the transition on the optical constants is reduced with W-doping (i.e., the difference between the n and k values at 20 °C and 100 °C is less for the films with a higher W/V cycle). The smooth transition between the two phases enables one to confidently extract the metallic fraction as a function of the temperature using the effective medium approximation (see Supporting Information Figure S7). Figure 2m presents the temperature evolution of the metallic fraction for the VO_2. The volumetric metallic fraction steadily increases with temperature following a sigmoid-like curve.

Fourier Transform Infrared Spectroscopy (FTIR) measurements were performed as a function of temperature for further characterizations of the optical properties. The optical properties of VO_2 modulated by W doping on the OSR stack of $VO_2/SiO_2/Al$ provide clear distinctions in infrared reflection, R, between the different material phases. Figure 3a–e show infrared absorption (1-R) spectra of W:VO_2 OSRs measured at various temperatures during cooling (see Supporting Information Figure S8 for heating curves). From the measured infrared spectra, emissivity can be calculated by averaging absorption weighted by the theoretical blackbody spectrum at the specific temperature (Figure 3f–j).

At 90 °C, the pure VO_2 sample (**Figure 3**a) has a broad infrared absorption due to its metallic properties in the infrared range, while below the transition the absorption drops sharply. Overall the spectral response remains the same with an increasing W/V ratio, but the transition point shifts to lower temperatures. The cold temperature absorption is also seen to slightly increase with W doping with visible absorption peaks ≈6 µm for W:VO_2 with higher W/V cycle ratios, indicating the optical contrast is reduced with the increase of W doping.

More detailed information on the hysteresis behavior can be seen in the IR emissivity plots. For pure VO_2 (Figure 3f), the transition temperature is extracted to be 71 °C and 55 °C for heating up (T_h) and cooling down (T_c), respectively. The transition temperature extraction is detailed in Supporting Information Figure S9. The figure shows an emissivity contrast $\Delta\varepsilon$ of 0.49. For the W:VO_2 samples (Figure 3g–j), the emissivity hysteresis curves clearly show that the transition temperature

© 2022 The Authors. Advanced Optical Materials published by Wiley-VCH GmbH

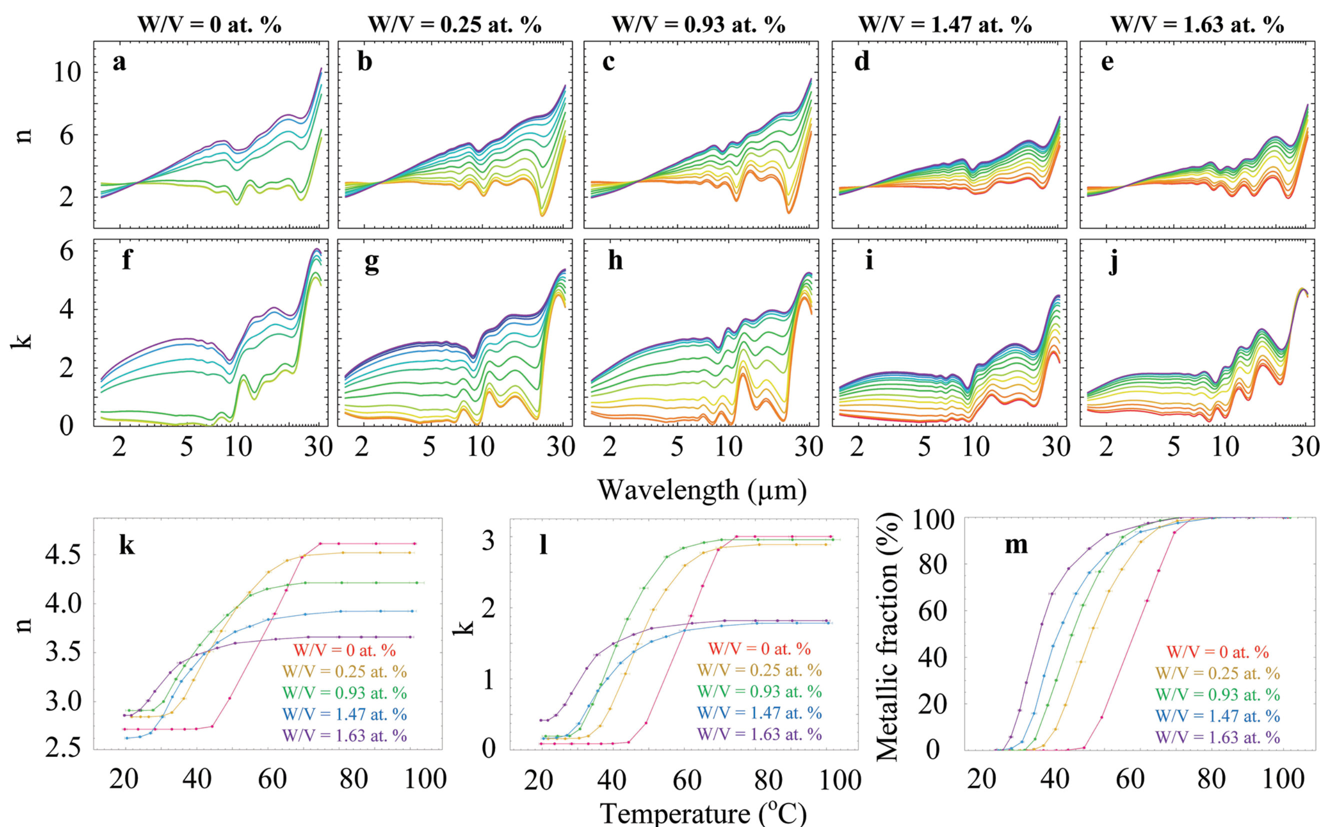

Figure 2. Infrared ellipsometry characterizations. a–e) n and f–j) k, respectively, for the VO_2 films with grown with W/V atomic ratio of a,f) 0%, b,g) 0.25%, c,h) 0.93%, d,i) 1.47%, and e, j) 1.63% at the different measured temperatures from 20 to 100 °C (dark red to purple lines), all data taken in the heating direction. k) n and l) k both at 5 µm wavelength, m) volumetric metallic fraction (from Bruggeman's effective medium approximation fitting) as a function of temperature for the W-doped VO_2 films for the VO_2 films with W/V atomic ratio of 0% (red line), 0.25% (yellow line), 0.93% (green line), 1.47% (blue line) and 1.63% (purple line).

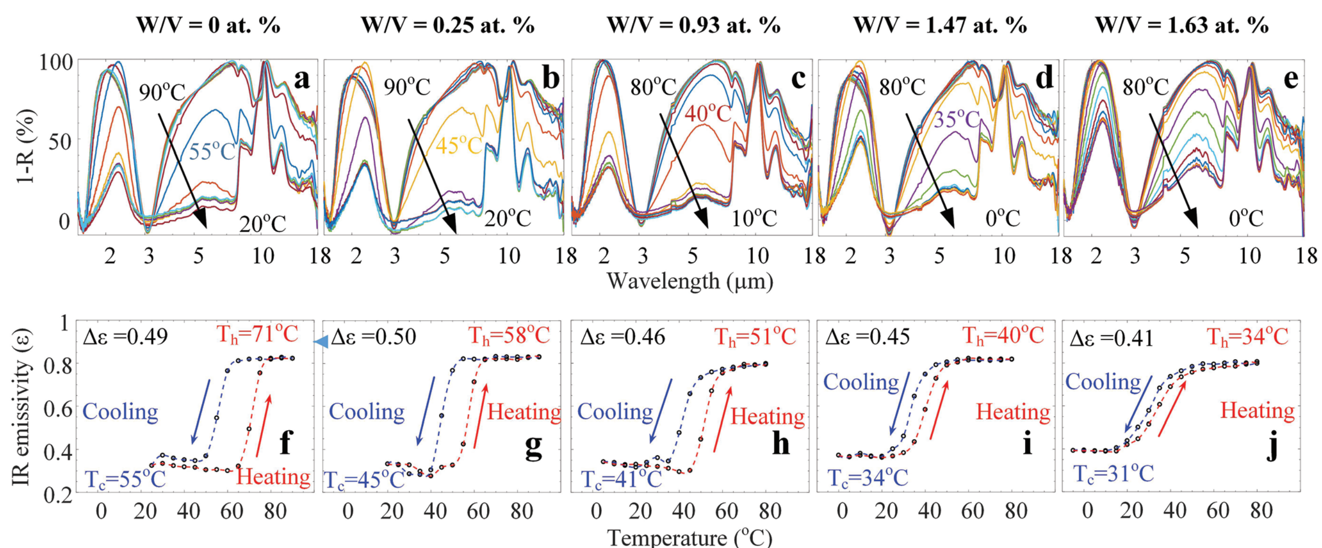

Figure 3. FTIR characterizations of deposited W:VO_2 film on SiO_2/Al stack. a–e) FTIR absorption spectra of W:VO_2 reflectors with different W contents at different temperatures (in cooling direction) for W/V ratio of a) 0 at.%, b) 0.25 at.%, c) 0.93 at.%, d) 1.47 at.% and e) 1.63 at.%. f–j) Full IR emissivity hysteresis curves (both heating and cooling) for the W:VO_2 reflectors with W/V ratio of f) 0 at.%, g) 0.25 at.%, h) 0.93 at.%, i) 1.47 at.% and j) 1.63 at.%.

© 2022 The Authors. Advanced Optical Materials published by Wiley-VCH GmbH

decreases with increasing W doping levels, while the emissivity reduces to 0.41 caused by an increase of the emissivity in the cold state. The temperature hysteresis, ΔT, gradually reduces with increasing W/V ratio, from a value of $\Delta T = 16$ °C for pure VO_2 to 3 °C for 1.63 at.% W doping. For the highest W/V ratios, the IMT transition loses some of its steepness and becomes more gradual in both directions of the heating and cooling cycles. To demonstrate the consistency of the ellipsometry and the FTIR data, the latter has been simulated using the transfer matrix method based on the extracted n and k values from the former. The simulated spectra are both qualitatively as well as quantitatively similar to each other. This is summarized in Supporting Information Figures S10 and S11.

Summarizing these results, we find that an increase of W doping in our ALD process allows to reduce the transition temperature in both heating and cooling cases, although at a cost of a small reduction in emissivity contrast. These trends of the ALD $W{:}VO_2$ films are consistent with those grown by other techniques, such as sputtering,[42] pulsed laser deposition,[23] and other chemical synthesis.[65] Therefore, the ALD technique can be used to grow $W{:}VO_2$ films with a modulation capability of electrical/optical properties and a transition temperature through tuning the W/V cycle ratio, matching physical methods of deposition for properties while maintaining the advantages of the atomic layer deposition process. Due to the constraint of the whole wafer anneal in our anneal facility, wafer scale uniformity has been confirmed by comparing chips of various parts of the wafer being anneal separately under the same circumstances. Comparing two nominally identical chips (Figures 3d/l and S11c/d), a variation of emissivity contrast of $\Delta\varepsilon$ is 0.03 observed while the variation in temperature transition between the chips is better than 1 °C.

To directly visualize the functionality of $W{:}VO_2$ and illustrate its application in control of thermal emissivity in the technologically important spectral bands of high atmospheric transmission, the IR thermochromic properties of the fabricated $W{:}VO_2$ optical solar reflectors were characterized using a Short- and Mid-Wave Infrared (MWIR) InSb camera with a spectral range of 1.5–5.1 µm. $W{:}VO_2$ samples were mounted on a hotplate with a stage temperature control together with four reference samples. Two samples consisting of respectively a carbon black tape (Agar Scientific) and a high carrier Al:ZnO (AZO) optical solar reflector (H-OSR),[66] are presented as high emissivity references. An uncoated Al mirror and a low carrier AZO OSR (L-OSR),[66] are presented as low emissivity references. Both AZO OSRs have similar conductive oxide/SiO_2/Al structures as the $W{:}VO_2$ samples, while the high carrier and low carrier AZO OSRs provide similar responses to $W{:}VO_2$ samples in the metallic and dielectric states, respectively. **Figure 4**a shows the

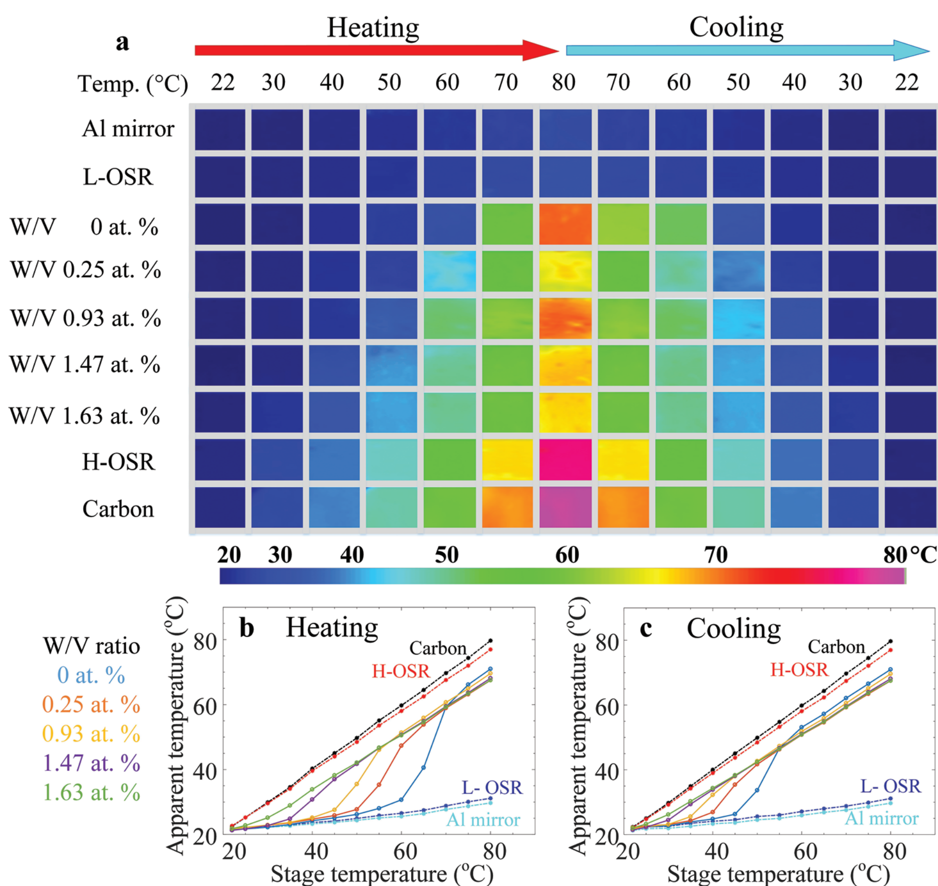

Figure 4. Apparent temperature characterization using a MWIR camera. a) Thermal image in MWIR (1.5–5.1 µm) band over a range of temperatures with $W{:}VO_2$ samples mounted on a hotplate, together with Carbon, Aluminum mirror, high emissivity AZO OSR and low emissivity AZO OSR as reference. b,c) Apparent temperature as a function of stage temperature during heating (b) and cooling (c).

© 2022 The Authors. Advanced Optical Materials published by Wiley-VCH GmbH

thermal images taken at different stage temperatures from a heating and cooling cycle. The individual sample images were cropped from the MWIR camera images with the original images presented in Supporting Information Figure S12. The measured apparent temperatures are plotted as a function of stage temperatures in Figure 4b for heating and 4c for cooling. The apparent temperatures of the carbon and H-OSR samples follow the stage temperature well due to their high MWIR emissivity. For the Al mirror and the L-OSR, the apparent temperatures are much lower than the stage temperature owing to their low IR emissivity. All reference samples follow a linear relation as their absorption is independent of temperature, unlike the different W:VO_2 (VO_2) materials. For pure VO_2 (W/V = 0 at.%), the apparent temperature is consistent with the L-OSR upon heating, until the temperature reaches 70 °C above which it then follows the H-OSR. For the cooling direction, the apparent temperature follows the H-OSR until the temperature reaches 65 °C, and subsequently follows the L-OSR. For the W:VO_2 films, similar trends of apparent temperature transitions between dielectric and metallic are seen, but at reduced temperatures in agreement with the transition temperatures extracted from Figure 3.

2.3. W:VO_2 Metasurface Optical Solar Reflectors on Polyimide Substrate

Besides integration into silicon technology, the application of W:VO_2 on flexible and conformable foils is of great interest for applications in thermochromic, energy management, and thermal control coatings. To explore the wider range of applications of the developed ALD W:VO_2 process as 'smart' metasurface optical solar reflector, the growth of W:VO_2 has therefore been investigated on flexible polyimide substrate. The W/V cycle configuration was set to 1.6, in order to reach the desired thermochromic phase transition close to room temperature. **Figure 5**a shows a photograph of a W:VO_2 coated 100 mm × 30 mm polyimide stripe after the post-deposition anneal at 375 °C, which was chosen for thermal compatibility with the polyimide (see details in the Experimental section). The polyimide sample retains its mechanical flexibility without any noticeable defects after the W:VO_2 growth and post-anneal, indicating the compatibility of the ALD W:VO_2 process with polyimide substrates. The infrared response characterized using FTIR results for absorption (1-R) are presented in Figure 5b as a function of temperature in the cooling direction from 70 °C to −10 °C. Similar to the W:VO_2 reflector on the Si substrate, the W:VO_2 reflector on polyimide substrate shows a significant IR absorption contrast between the cold and hot states. The low-temperature absorption ≈5 μm is higher than the values shown in Figure 3, which is attributed to the higher W/V cycle ratio of the W:VO_2/polyimide sample. Figure 5c shows the full IR emissivity hysteresis as a function of temperature of the W:VO_2 reflector on polyimide substrate. The heating and cooling transition temperatures are extracted as 30 °C and 25 °C, respectively. The IR emissivity contrast was extracted to be $\Delta\varepsilon = 0.39$, similar to the contrast of $\Delta\varepsilon = 0.42$ seen on Si substrate (Supporting Information Figure S13), indicating that W:VO_2 optical contrast is little affected by deposition on polyimide substrates.

Through photolithography and ion beam etching (see Supporting Information Figure S14), VO_2 meta-OSRs were fabricated on a 30 × 30 mm^2 polyimide substrate and presented as

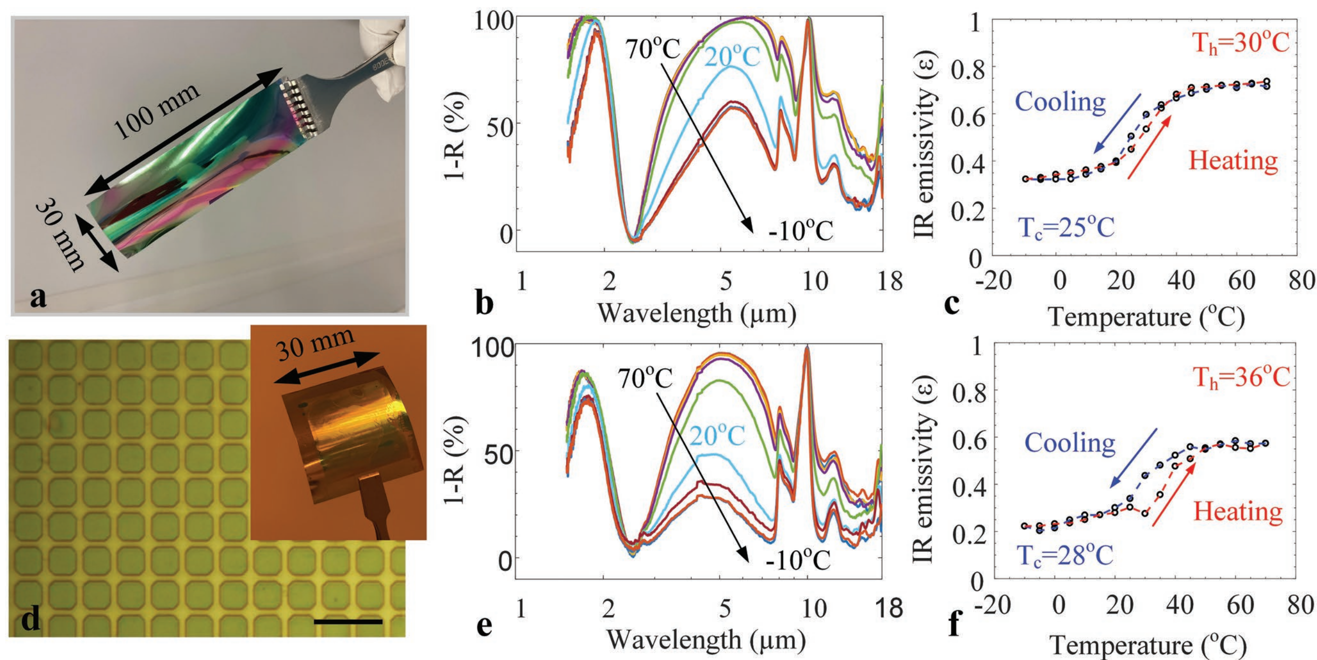

Figure 5. ALD W:VO_2 meta-surface formed on a flexible polyimide substrate. a) Photograph of WVO_2 grown on a polyimide stripe, b) FTIR absorption spectra of the W:VO_2 reflectors on polyimide at different temperatures (cooling), c) IR emissivity hysteresis curve extracted from FTIR spectra. d) Optical micrograph of WVO_2 metasurface patterned using photolithography (scale bar 10 μm, photograph as inset), e) FTIR absorption spectra of the W:VO_2 metasurface reflectors on polyimide at different temperatures (cooling), and f) IR emissivity hysteresis curve extracted of W:VO_2 metasurface reflectors.

© 2022 The Authors. Advanced Optical Materials published by Wiley-VCH GmbH

Nomarski micrograph in Figure 5d with a photo as inset. The metasurface is formed by 3.5 µm wide square WVO_2 features and 1.5 µm gaps between features. The IR absorption spectra is presented in Figure 5e as a function of temperature (cooling from 70 °C to –10 °C) and IR emissivity hysteresis is shown in Figure 5f. Similar to the W:VO_2 planar reflector, the W:VO_2 meta-OSR shows a significant IR absorption contrast between the cold and hot status. The IR emissivity contrast is 0.35, which is slightly lower than the unpatterned film but at a significantly reduced W:VO_2 coverage of 49%. The reduced W:VO_2 coverage is highly desirable for its lower solar absorption as previously demonstrated.[12] These results are consistent with film and metasurface OSRs on Si substrate (see Supporting Information S13). Therefore, the novel ALD W:VO_2 process is fully compatible with flexible substrates, allowing room temperature smart transitions with a large emissivity contrast for large area flexible substrate applications. The W:VO_2 ALD process opens up novel applications including gradient W:VO_2 stacks[23] because of the ability of ALD to accurately control the doping in situ while maintaining an excellent control of thickness.

3. Conclusion

In summary, we report a large area atomic layer deposition process to grow tungsten-doped vanadium dioxide (W:VO_2) on 200 mm Si substrates. The tungsten content in the W:VO_2 film can be accurately defined through the cycle ratio of tungsten and vanadium precursors. Through optical characterizations, the transition temperature is demonstrated to be dependent on the incorporated W doping. The increase of W doping reduces both the transition temperature and hysteresis of the phase transition reaching room temperature at ≈1.63 at.% W. The reduction in optical properties contrasts of the W:VO_2 films with increasing W-doping is limited and allows phase transition operation near room temperature. We demonstrated the W:VO_2 can be formed on flexible polyimide substrates through an optimized lower post-anneal temperature and the fabricated W:VO_2 meta-OSR demonstrates a near room temperature transition capability with a large IR emissivity contrast. Atomic-layer deposition of W:VO_2 is an enabling technology offering a production-level CMOS-compatible route toward thermochromic and energy saving coatings on flexible polyimide substrates as well as non-volatile switchable devices on silicon.

4. Experimental Section

W-Doped VO_2 by Atomic Layer Deposition and its Post-Deposition Anneal: The VO_2 ALD process was carried out using Tetrakis(ethylmethylamino) vanadium(IV) (TEMAV) 98% from Strem Chemicals and deionized water as oxidizer. For the WO_x process, the precursor Tungsten hexacarbonyl ($W(CO)_6$) 99% from Strem Chemicals and deionized water were used. All films were deposited at 200 °C in a Savannah S200 ALD system. For 40 nm thick VO_2 on Si substrates, the growth cycle number was set to be 1100 and the same number was used for W:VO_2 with various W/V cycle ratio of 0.2, 0.6, 0.8, and 1.2. The VO_2 is deposited as an amorphous film and a post-deposition anneal is required to form crystalline VO_2(M1). The anneal was done in an Oxford Instruments Agile NanoFab CVD system, which has the capability of the oxygen flow, vacuum, and anneal temperature compatibility. Different anneal conditions were performed to achieve VO_2 with transition capability and the anneal condition was found to be optimized at 400 °C, oxygen partial pressure of 133 Pa, and duration of 2 hours.

Fabrication of W-Doped VO_2 Meta-OSRs on Polyimide Substrates: A 100 nm Al and 900 nm SiO_2 was formed on a polyimide substrate (DuPont Kapton) using sputtering. About 45 nm W:VO_2 with a W/V cycle ratio of 1.6 was subsequently grown on top of the SiO_2. After deposition a post-deposition anneal at 375 °C for 2 h at 533 Pa pressure with a O_2/Ar mixture of 1:1. The polyimide substrate was then mounted on a methyl methacrylate (MMA) coated Si carrier wafer with the MMA as an adhesive. The sample with MMA was then baked for 1 min at 120 °C and Shipley 1813 photoresist was coated, baked and exposed using a contact aligner EVG 6200. The W:VO_2 was subsequently etched in an Oxford Instrument IonFab 300 plus through an Ar beam etch using cycled etch of 15 s and cooling of 1 min to avoid resist overheat. The etch parameters are available in our previous work.[67] The photoresist was subsequently removed using an ultrasonic bath in NMP at 60 °C. The polyimide was also unmounted during the NMP bath. The fabrication process is detailed in Supporting Information Figure S14.

Material Characterizations: The W:VO_2 thickness mapping was measured at room temperature immediately after deposition using a Woollam M2000 Ellipsometer with a measurement range from 0.2 to 1.7 µm at an incident angle of 75°. VO_2 was characterized in a Thermo Scientific Theta Probe X-ray photoelectron spectroscopy (XPS) system in ultrahigh vacuum conditions (base pressure $P \approx 1.0 \times 10^{-7}$ Pa). No argon etch was performed as it is known to preferentially remove oxygen atoms, which in turn affects the vanadium oxide stoichiometry.[55] The XPS data was analyzed using Themo Avantage software. After the post-deposition anneal, W:VO_2 (and VO_2) were characterized using a Renishaw inVia laser Raman spectrometer using 532 nm laser with the exposure power set at below 0.1 mW to avoid film heating. For the room temperature Raman measurements, all samples were seated on the stage in air. For temperature sweeps, the samples were mounted on the heater in a Nanonics CryoView CV2000 system. During the measurement, the system was under vacuum of 1.3×10^{-3} Pa. The Raman signal was taken more than 1 minute after temperature stabilization.

Optical Characterizations: Infrared reflectance was measured over the range of 1.6 to 18 µm using a Fourier transform infrared microscopy (FTIR, Thermo-Nicolet Nexus 670, Continuum microscope) using a × 15 optical objective (numerical aperture 0.58) and MCT-A detector. The KBr beam splitter and IR source were used, and the transmittance and reflectance were normalized with air and an aluminum mirror, respectively. The sample temperature was controlled by mounting the sample on the stage of Linkam THMS600 with a ZnS window and the below room-temperature measurements were carried out using liquid nitrogen cooling. The reflection reference was based on an Al mirror. Measurements were performed after 1 min temperature stabilization. The temperature sweep was carried out by a cool down and then heat up.

The MWIR images were taken through a CEDIP/FLIR IR camera Titanium SC7200 using an InSb detector with a range of 1.5–5.1 µm. The W:VO_2 samples with different W/V ratios were mounted on a hotplate through double-sided sticky copper tapes (see Supporting Information Figure S12). Four references were also mounted with carbon and high carrier AZO OSR (H-OSR) as high emissivity and Al mirror and low carrier AZO OSR (L-OSR) as low emissivity. Further details of these two AZO OSRs are available in previous work.[66] The IR image measurements were taken with the stage set at temperatures from 22 to 80 °C and then down to 22 °C with step of 5 °C. The data were analyzed using FLIR Altair.

IR Ellipsometry: Ellipsometric Data Acquisition Optical characterization, under various temperatures (20–100 °C) was performed using a J. A. Woollam Mark II infrared (IR) spectroscopic ellipsometer (SE) in the spectral range of 1.55–30 µm at an incident angle of 75°, to measure the ellipsometric angles $\Phi(E)$ and $\Delta(E)$. A custom-built stage was used to allow for measurements above room temperature. A heat gun was positioned at ≤ 10 cm from the sample at an angle of 45°. An IR thermal imaging camera monitored the temperature of the VO_2 film. The camera was independently cross-calibrated by measuring the sample surface at 20–100 °C on top of a calibrated hotplate.

© 2022 The Authors. Advanced Optical Materials published by Wiley-VCH GmbH

Optical Solar Reflector Performance Extraction: According to Kirchhoff's law, the spectral emissivity and spectral absorptance of a body are equal at thermal equilibrium condition. For an IR opaque reflector without transmission, the emissivity, $\varepsilon(\lambda)$, can be described using the relation: $\varepsilon(\lambda) = 1 - R(\lambda)$, where $R(\lambda)$ is the reflectivity. The emissivity is defined as the averaging absorption weighted by the theoretical blackbody spectrum at the operating temperature (T) in Kelvin:[68]

$$\varepsilon = \frac{\int (1-R(\lambda))B(\lambda,T)d\lambda}{\int B(\lambda,T)d\lambda} \tag{1}$$

where $B(\lambda, T)$ is the blackbody spectral distribution at temperature T, given by Planck's equation. In this work, the integration range is the set FTIR measurement range from 2.5 to 18 µm owning to the measurable range of the FTIR system. In the calculation, T is set as the set temperature of measurements.

Supporting Information

Supporting Information is available from the Wiley Online Library or from the author.

Acknowledgements

This project has received funding from the European Union's Horizon 2020 research and innovation program under Grant Agreement No. 821932 "SMART-FLEX". O.M. acknowledges support from EPSRC grant EP/M009122/1. K.S. acknowledges Oxford Instruments Plasma Technology (OIPT) for its support of PlasmaPro 100 Nano system configuration for VO_2 anneals and useful discussions with Dr Mike Cooke from OIPT.

Conflict of Interest

The authors declare no conflict of interest.

Data Availability Statement

The data that support the findings of this study are openly available in the University of Southampton at https://doi.org/10.5258/SOTON/D2198, reference number 2198.

Keywords

atomic layer deposition, metasurfaces, optical solar reflector, radiative cooling, vanadium dioxide

Received: June 8, 2022
Revised: August 27, 2022
Published online:

[1] F. J. Morin, *Phys. Rev. Lett.* **1959**, *3*, 34.
[2] Q. Hao, W. Li, H. Xu, J. Wang, Y. Yin, H. Wang, L. Ma, F. Ma, X. Jiang, O. G. Schmidt, P. K. Chu, *Adv. Mater.* **2018**, *30*, 1705421.
[3] J. Schläefer, C. Sol, T. Li, D. Malarde, M. Portnoi, T. J. Macdonald, S. K. Laney, M. J. Powell, I. Top, I. P. Parkin, I. Papakonstantinou, *Sol. Energy Mater Sol., C* **2019**, *200*, 109944.
[4] E. Gagaoudakis, E. Aperathitis, G. Michail, M. Panagopoulou, D. Katerinopoulou, V. Binas, Y. S. Raptis, G. Kiriakidis, *Sol. Energy* **2018**, *165*, 115.
[5] Y. Cui, Y. Ke, C. Liu, Z. Chen, N. Wang, L. Zhang, Y. Zhou, S. Wang, Y. Gao, Y. Long, *Joule* **2018**, *2*, 1707.
[6] S. Chen, Z. Wang, H. Ren, Y. Chen, W. Yan, C. Wang, B. Li, J. Jiang, C. Zou, *Sci. Adv.* **2019**, *5*, eaav6815.
[7] S. J. Lee, D. S. Choi, S. H. Kang, W. S. Yang, S. Nahm, S. H. Han, T. Kim, *ACS Sustainable Chem. Eng.* **2019**, *7*, 7111.
[8] M. Li, S. Magdassi, Y. Gao, Y. Long, *Small* **2017**, *13*, 1701147.
[9] M. Aburas, V. Soebarto, T. Williamson, R. Liang, H. Ebendorff-Heidepriem, Y. Wu, *Appl. Energy* **2019**, *255*, 113522.
[10] M. Ono, K. Chen, W. Li, S. Fan, *Opt. Express* **2018**, *26*, A777.
[11] M. Chen, A. M. Morsy, M. L. Povinelli, *Opt. Express* **2019**, *27*, 21787.
[12] K. Sun, C. A. Riedel, A. Urbani, M. Simeoni, S. Mengali, M. Zalkovskij, B. Bilenberg, C. H. de Groot, O. L. Muskens, *ACS Photonics* **2018**, *5*, 2280.
[13] A. M. Morsy, M. T. Barako, V. Jankovic, V. D. Wheeler, M. W. Knight, G. T. Papadakis, L. A. Sweatlock, P. W. C. Hon, M. L. Povinelli, *Sci. Rep.* **2020**, *10*, 13964.
[14] E. Corti, B. Gotsmann, K. Moselund, A. M. Ionescu, J. Robertson, S. Karg, *Solid-State Electron.* **2020**, *168*, 107729.
[15] J. Núñez, M. J. Avedillo, M. Jiménez, J. M. Quintana, A. Todri-Sanial, E. Corti, S. Karg, B. Linares-Barranco, *Front Neurosci* **2021**, *15*.
[16] S.-H. Bae, S. Lee, H. Koo, L. Lin, B. H. Jo, C. Park, Z. L. Wang, *Adv. Mater.* **2013**, *25*, 5098.
[17] L. Pellegrino, N. Manca, T. Kanki, H. Tanaka, M. Biasotti, E. Bellingeri, A. S. Siri, D. Marré, *Adv. Mater.* **2012**, *24*, 2929.
[18] Y. Jung, J. Jeong, Z. Qu, B. Cui, A. Khanda, S. S. P. Parkin, J. K. S. Poon, *Adv. Electron. Mater.* **2021**, *7*, 2001142.
[19] R. Matos, N. Pala, *Sci. Rep.* **2022**, *12*, 4497.
[20] B. Gerislioglu, A. Ahmadivand, M. Karabiyik, R. Sinha, N. Pala, *Adv. Electron. Mater.* **2017**, *3*, 1700170.
[21] X. Duan, S. T. White, Y. Cui, F. Neubrech, Y. Gao, R. F. Haglund, N. Liu, *ACS Photonics* **2020**, *7*, 2958.
[22] H. J. Kim, Y. H. Choi, D. Lee, I. H. Lee, B. K. Choi, S.-H. Phark, Y. J. Chang, *Appl. Surf. Sci.* **2021**, *561*, 150056.
[23] K. Tang, X. Wang, K. Dong, Y. Li, J. Li, B. Sun, X. Zhang, C. Dames, C. Qiu, J. Yao, J. Wu, *Adv. Mater.* **2020**, *32*, 1907071.
[24] Z. Xu, Q. Li, K. Du, S. Long, Y. Yang, X. Cao, H. Luo, H. Zhu, P. Ghosh, W. Shen, M. Qiu, *Laser Photonics Rev.* **2020**, *14*, 1900162.
[25] Y.-G. Jeong, S. Han, J. Rhie, J.-S. Kyoung, J.-W. Choi, N. Park, S. Hong, B.-J. Kim, H.-T. Kim, D.-S. Kim, *Nano Lett.* **2015**, *15*, 6318.
[26] Y. F. Wu, L. L. Fan, S. M. Chen, S. Chen, C. W. Zou, Z. Y. Wu, *AIP Adv.* **2013**, *3*, 042132.
[27] M. Tangirala, K. Zhang, D. Nminibapiel, V. Pallem, C. Dussarrat, W. Cao, T. N. Adam, C. S. Johnson, H. E. Elsayed-Ali, H. Baumgart, *ECS J. Solid State Sci. Technol.* **2014**, *3*, N89.
[28] H.-T. Zhang, L. Zhang, D. Mukherjee, Y.-X. Zheng, R. C. Haislmaier, N. Alem, R. Engel-Herbert, *Nat. Commun.* **2015**, *6*, 8475.
[29] A. P. Peter, K. Martens, G. Rampelberg, M. Toeller, J. M. Ablett, J. Meersschaut, D. Cuypers, A. Franquet, C. Detavernier, J.-P. Rueff, M. Schaekers, S. Van Elshocht, M. Jurczak, C. Adelmann, I. P. Radu, *Adv. Funct. Mater.* **2015**, *25*, 679.
[30] M. Currie, M. A. Mastro, V. D. Wheeler, *J Vis Exp* **2018**, e57103.
[31] P. A. Premkumar, M. Toeller, I. P. Radu, C. Adelmann, M. Schaekers, J. Meersschaut, T. Conard, S. V. Elshocht, *ECS J. Solid State Sci. Technol.* **2012**, *1*, P169.
[32] G. Rampelberg, M. Schaekers, K. Martens, Q. Xie, D. Deduytsche, B. D. Schutter, N. Blasco, J. Kittl, C. Detavernier, *Appl. Phys. Lett.* **2011**, *98*, 162902.
[33] K. Sun, W. Xiao, C. Wheeler, M. Simeoni, A. Urbani, M. Gaspari, S. Mengali, C. H. d. Groot, O. L. Muskens, *Nanophotonics* **2022**, *11*, 4101.

© 2022 The Authors. Advanced Optical Materials published by Wiley-VCH GmbH

[34] Z. Li, J. Wu, Z. Hu, Y. Lin, Q. Chen, Y. Guo, Y. Liu, Y. Zhao, J. Peng, W. Chu, C. Wu, Y. Xie, *Nat. Commun.* **2017**, *8*, 15561.
[35] M. M. Qazilbash, M. Brehm, B.-G. Chae, P.-C. Ho, G. O. Andreev, B.-J. Kim, S. J. Yun, A. V. Balatsky, M. B. Maple, F. Keilmann, H.-T. Kim, D. N. Basov, *Science* **2007**, *318*, 1750.
[36] K. Liu, S. Lee, S. Yang, O. Delaire, J. Wu, *Mater. Today* **2018**, *21*, 875.
[37] D. Kolenatý, J. Vlček, T. Bárta, J. Rezek, J. Houška, S. Haviar, *Sci. Rep.* **2020**, *10*, 11107.
[38] B. Li, S. Tian, Z. Wang, B. Liu, X. Gong, X. Zhao, *Appl. Surf. Sci.* **2021**, *568*, 150959.
[39] Z. Wen, Y. Ke, C. Feng, S. Fang, M. Sun, X. Liu, Y. Long, *Adv. Mater. Interfaces* **2021**, *8*, 2001606.
[40] A. V. Ivanov, A. Y. Tatarenko, A. A. Gorodetsky, O. N. Makarevich, M. Navarro-Cía, A. M. Makarevich, A. R. Kaul, A. A. Eliseev, O. V. Boytsova, *ACS Appl. Nano Mater.* **2021**, *4*, 10592.
[41] C. Ling, Z. Zhao, X. Hu, J. Li, X. Zhao, Z. Wang, Y. Zhao, H. Jin, *ACS Appl. Nano Mater.* **2019**, *2*, 6738.
[42] G. Karaoglan-Bebek, M. N. F. Hoque, M. Holtz, Z. Fan, A. A. Bernussi, *Appl. Phys. Lett.* **2014**, *105*, 201902.
[43] D. Liu, H. Cheng, X. Xing, C. Zhang, W. Zheng, *Infrared Phys. Technol.* **2016**, *77*, 339.
[44] K. N. Marshall, R. A. Breuch, *J Spacecr Rockets* **1968**, *5*, 1051.
[45] K. Sun, C. A. Riedel, Y. Wang, A. Urbani, M. Simeoni, S. Mengali, M. Zalkovskij, B. Bilenberg, C. H. de Groot, O. L. Muskens, *ACS Photonics* **2018**, *5*, 495.
[46] D. U. Yildirim, A. Ghobadi, M. C. Soydan, O. Atesal, A. Toprak, M. D. Caliskan, E. Ozbay, *ACS Photonics* **2019**, *6*, 1812.
[47] K. M. Martens, I. P. Radu, G. Rampelberg, J. Verbruggen, S. Cosemans, S. Mertens, X. Shi, M. Schaekers, C. Huyghebaert, S. De-Gendt, C. Detavernier, M. Heyns, J. A. Kittl, *ECS Trans.* **2012**, *45*, 151.
[48] H. H. Park, T. J. Larrabee, L. B. Ruppalt, J. C. Culbertson, S. M. Prokes, *ACS Omega* **2017**, *2*, 1259.
[49] G. Bai, K. M. Niang, J. Robertson, *J, Vac. Sci. Technol. A* **2020**, *38*, 052402.
[50] M. A. Mamun, K. Zhang, H. Baumgart, A. A. Elmustafa, *ECS J. Solid State Sci. Technol.* **2015**, *4*, P398.
[51] J. Malm, T. Sajavaara, M. Karppinen, *Chem. Vap. Deposition* **2012**, *18*, 245.
[52] V. P. Prasadam, N. Bahlawane, F. Mattelaer, G. Rampelberg, C. Detavernier, L. Fang, Y. Jiang, K. Martens, I. P. Parkin, I. Papakonstantinou, *Mater. Today Chem.* **2019**, *12*, 396.
[53] A. C. Kozen, H. Joress, M. Currie, V. R. Anderson, C. R. Eddy, V. D. Wheeler, *J. Phys. Chem. C* **2017**, *121*, 19341.
[54] F. Mattelaer, K. Geryl, G. Rampelberg, T. Dobbelaere, J. Dendooven, C. Detavernier, *RSC Adv.* **2016**, *6*, 114658.
[55] E. Hryha, E. Rutqvist, L. Nyborg, *Surf. Interface Anal.* **2012**, *44*, 1022.
[56] F. Ureña-Begara, A. Crunteanu, J.-P. Raskin, *Appl. Surf. Sci.* **2017**, *403*, 717.
[57] M. Vasilopoulou, A. Soultati, D. G. Georgiadou, T. Stergiopoulos, L. C. Palilis, S. Kennou, N. A. Stathopoulos, D. Davazoglou, P. Argitis, *J. Mater. Chem. A* **2014**, *2*, 1738.
[58] S.-E. Chen, H.-H. Lu, S. Brahma, J.-L. Huang, *Thin Solid Films* **2017**, *644*, 52.
[59] E. Z. Kurmaev, V. M. Cherkashenko, Y. M. Yarmoshenko, S. Bartkowski, A. V. Postnikov, M. Neumann, L. C. Duda, J. H. Guo, J. Nordgren, V. A. Perelyaev, W. Reichelt, *J. Phys.: Condens. Matter* **1998**, *10*, 4081.
[60] Y. Schuhl, H. Baussart, R. Delobel, M. Le Bras, J.-M. Leroy, L. Gengembre, J. Grimblot, *J. Chem. Soc., Faraday Trans. 1* **1983**, *79*, 2055.
[61] Y. Huang, D. Zhang, Y. Liu, J. Jin, Y. Yang, T. Chen, H. Guan, P. Fan, W. Lv, *Appl. Surf. Sci.* **2018**, *456*, 545.
[62] C.-Y. Kim, T. Slusar, J. Cho, H.-T. Kim, *ACS Appl. Electron. Mater.* **2021**, *3*, 605.
[63] J. A. Ramirez-Rincon, C. L. Gomez-Heredia, A. Corvisier, J. Ordonez-Miranda, T. Girardeau, F. Paumier, C. Champeaux, F. Dumas-Bouchiat, Y. Ezzahri, K. Joulain, O. Ares, J. J. Alvarado-Gil, *J. Appl. Phys.* **2018**, *124*, 195102.
[64] H. G. H. J. N. Tompkins, *Spectroscopic Ellipsometry: Practical Application to Thin Film Characterization*, Momentum Press, New York **2016**.
[65] J. Zou, X. Chen, L. Xiao, *Mater. Res. Express* **2018**, *5*, 065055.
[66] K. Sun, W. Xiao, S. Ye, N. Kalfagiannis, K. S. Kiang, C. H. de Groot, O. L. Muskens, *Adv. Mater.* **2020**, *32*, 2001534.
[67] K. Sun, I. Zeimpekis, C. Hu, N. M. J. Ditshego, O. Thomas, M. R. R. de Planque, H. M. H. Chong, H. Morgan, P. Ashburn, *Microelectron. Eng.* **2016**, *153*, 96.
[68] R. A. Breuch, K. N. Marshall, *J Spacecr Rockets* **1968**, *5*, 1051.

© 2022 The Authors. Advanced Optical Materials published by Wiley-VCH GmbH